# Polymorphism in N,N'-dialkyl-naphthalene diimides†

Silvia Milita,*[a] Fabiola Liscio,[a] Lewis Cowen,[b] Massimiliano Cavallini,[c] Ben A. Drain,[d] Thibault Degousée,[e,f] Sally Luong,[e,f] Oliver Fenwick,[e,f] Antonietta Guagliardi,[g] Bob C. Schroeder,[b] Norberto Masciocchi*[h]

Received 00th January 20xx,
Accepted 00th January 20xx

DOI: 10.1039/x0xx00000x

The long-known class of compounds called naphthalene diimides (NDI), bearing alkyl subtituents on the imide nitrogen atoms, have been widely used as active materials in thin film devices with interesting optical, sensing and electrical applications. Less is known about their rich crystal chemical behaviour, which comprises numerous polymorphic transitions, and the occurrence of elusive liquid crystalline phases. It is this behaviour which determines the response of the devices based on them. Here we fully characterized, by combining a combination of differential scanning calorimetry, powder and thin film diffraction and optical microscopy techniques, two newly synthetized NDI materials bearing *n*-octyl and *n*-decyl side-chains, as well as lighter analogues, of known room temperature crystal structures. In search for a rationale of their physico-chemical properties, phase stability and thermally induced solid-state transition reversibility the differential behaviour of these NDI materials is here interpreted based on the competitive role of intermolecular π-π interactions and of the alkyl chains flexibility. The occurrence of comparable local minima of the molecular conformational energy hypersurface for shorter alkyls, and for longer ones of rotator phases, is here invoked.

## 1. Introduction

After several years of fundamental studies, flexible organic and bio-electronics have entered the market as displays and devices, recently incorporated into large commodities available to the wider public.[1] Synthetic and material chemists assisted this lively and rapidly evolving field by preparing molecular systems to be used as key building blocks for optoelectronics, computing, and sensing devices.[2] In contrast to the conventional electronics based on inorganics, organic semiconductors take advantage of electronically-active carbon-based self-assemblies or macro-molecules, providing solution-processable, flexible, adjustable and cost efficient devices. Elegant examples of organic electronic applications include OLED cell phone displays, flexible light panels, rollable solar cells, and battery-free artificial retina.[3] Among other recent applications, the possibility of building low-temperature thermoelectric generators[4] for energy recovery from mild heat sources has been tackled. In this case the success relies in optimizing concurrently different properties (such as the electrical and thermal conductivity, the Seebeck coefficient and the chemical and thermal stability) in order to obtain high performing devices by easily processable methods.

While excellent device performances have been obtained for p-type organic semiconductors the n-type air instability, typical for these systems although not ubiquitous, markedly affects the electron transport due to the detrimental effect of oxygen molecules.[5] For this reason a big effort is still devoted to developing appealing n-type organic semiconductors.[6] Among the most studied n-type systems N-alkyl substituted PDI materials (PDI = N,N'-dialkyl-perylene diimides) have been demonstrated to meet several requirements such as air stability, processability and high charge carrier mobility at once.[7] They have shown excellent chemical, thermal, and optical stabilities as well as high luminescence efficiencies and remarkable optoelectronic properties.[8] They have been successfully employed in the production of field effect transistors, photovoltaic devices and dye lasers.[9] NDI (NDI = N,N'-naphthalene diimides) analogues are structurally simpler and cheaper. Thanks to their enhanced solubility they are more easily processable; accordingly they have been widely studied in the form of both bulk and films.[10] Their applications sweeping from sensors, molecular switching, catalysis and use in medicinal and electronic devices.[11] Notwithstanding investigations on how to prepare NDI-based derivatives and polymers with appreciable power conversion efficiencies in photovoltaic applications fall in a still rapidly growing field.

Semiconducting organic films based on NDI and PDI polyaromatic rings, properly stacked within films and possibly doped with exogenous species (ions, nanoparticles, etc.), are promising materials. They do, however, suffer from intrinsic structural versatility in that several polymorphs can be formed (in the bulk) with little control on the actual structure type being obtained upon film deposition and processing. In addition novel polymorphs can be also be induced by the substrate surface depending on the deposition technique.[12] In the specific case of NDI congeners the occurrence of polymorphism has been reported,[13] but the structural features behind the phenomenon are still unknown.

While having the same chemical composition each polymorph is unique with its own physical and chemical properties. Owing

[a] *Istituto per la Microelettronica e Microsistemi, Consiglio Nazionale delle Ricerche, via Gobetti 101, 40129 Bologna, Italy, milita@bo.imm.cnr.it.*
[b] *Department of Chemistry, University College London, London WC1H 0AJ, UK*
[c] *Istituto per lo Studio dei Materiali Nanostrutturati, Consiglio Nazionale delle Ricerche, via Gobetti 101, 40129 Bologna, Italy*
[d] *Department of Chemistry, University of Warwick, Coventry CV4 7AL, UK*
[e] *School ofEngineering and Materials Sciences, Queen Mary University of London, London E1 4NS, UK.*
[f] *The Organic Thermoelectrics Laboratory, Materials Research Institute, Queen Mary University of London, London E1 4NS, UK.*
[g] *Istituto di Cristallografia & To.Sca.Lab., Consiglio Nazionale delle Ricerche, via Valleggio 11, 22100 Como, Italy*
[h] *Dipartimento di Scienza e Alta Tecnologia & INSTM., Università dell'Insubria, via Valleggio 11, 22100 Como, Italy, norberto.masciocchi@uninsubria.it.*
S.M and F.L. equally contributed to this work

† Electronic Supplementary Information (ESI) available: NMR, UV-Vis absorption spectra, XRPD, POM and AFM details, two POM movies. See DOI: 10.1039/x0xx00000x

to these differences understanding and controlling polymorph formation of organic compounds is of interest in pharmaceutical industries,[14] organic electronics and in functional materials in general.[15] In particular in small molecule organic semiconductors the crystal structure is crucial for device performance.[16]

In this work we focus our attention on a prototype system, i.e. symmetrically substituted linear dialkyl NDI. The studied series consists of four molecular *n*-alkylated NDI derivatives with *n*-butyl, *n*-hexyl, *n*-octyl and *n*-decyl side-chains respectively (see Chart 1). As later detailed we employed structural powder diffraction methods, thermal analyses, variable temperature diffraction methods, optical imaging and grazing-incidence X-ray diffraction of spin-coated films to unravel the rich polymorphic landscape.

To better convey the labelling used throughout this paper, NDIx refers to NDI molecules bearing *n*-alkyl $C_xH_{2x+1}$ chains; x$\alpha$,…,x$\delta$ indicate different polymorphic phases of the NDIx species (starting from the low-temperature ones) and LC labels a liquid crystalline mesophase formed at temperature slightly lower than the melting point (m.p.).

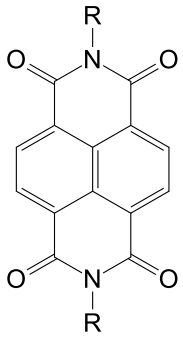

R = *n*-butyl for NDI4

R = *n*-hexyl for NDI6

R = *n*-octyl for NDI8

R = *n*-decyl for NDI10

**Chart I.** Chemical structure of NDIx molecules.

## 2. Experimental Section

**(a) Materials**

All chemicals were purchased from commercial suppliers and used without further purification.

**(b) Synthesis of the NDI compounds**

The different *N,N'*-dialkyl-naphthalene diimides compounds were prepared according to modified literature procedures.[17]

**N,N'-Dibutyl-1,4,5,8-naphthalenetetracarboxylic 1,8:4,5-di imide (NDI4):** A mixture of 1,4,5,8-Naphthalenetetracarbo xylic dianhydride (2.00 g, 7.5 mmol) and *n*-butylamine (3.00 mL, 29.8 mmol) were added to acetic acid (30 mL). The resulting suspension was stirred at 100 °C overnight. After cooling to room temperature, the solids were collected by filtration and washed with cold methanol. The crude product was recrystallised from a mixture of dichloromethane and methanol to yield the title compound as pale yellow crystals (2.52 g, 6.7 mmol, 89%). $^1$H NMR (400 MHz, $CDCl_3$, 25 °C) $\delta$ 8.72 (s, 4H), 4.19 (t, *J* = 7.2 Hz, 4H), 1.77 – 1.67 (m, 4H), 1.51 – 1.39 (m, 4H), 0.98 (t, *J* = 7.4 Hz, 6H). $^{13}$C NMR (100 MHz, $CDCl_3$, 25 °C) $\delta$ 162.9, 131.0, 126.8, 126.8, 40.9, 30.3, 20.5, 13.9.

**N,N'-Dihexyl-1,4,5,8-naphthalenetetracarboxylic 1,8:4,5-diimide (NDI6):** 1,4,5,8-Naphthalenetetracarboxylic dianhydride (1.00 g, 3.7 mmol) and *n*-hexylamine (2.00 mL, 15.1 mmol) were dissolved in dimethylformamide (30 mL) and heated to 120 °C overnight. The dark red reaction mixture was cooled to room temperature, water (50 mL) was added and the mixture extracted with dichloromethane (3 × 50 mL). The combined organic layers were washed with water (2 × 100 mL), dried over magnesium sulphate, filtered and the solvent evaporated. The red crude solid was then recrystallised from a mixture of dichloromethane and methanol. The final product was recovered as pink needles (1.20 g, 2.8 mmol, 74%). $^1$H NMR (700 MHz, $CDCl_3$, 25 °C) $\delta$ 8.74 (s, 4H), 4.19 (t, *J* = 7.2 Hz, 4H), 1.74 (quin, 4H), 1.44 (quin, 4H), 1.38-1.31 (m, 8H), 0.90 (t, 6H); $^{13}$C NMR (175 MHz, $CDCl_3$, 25 °C) $\delta$ 162.9, 131.0, 126.8, 41.1, 31.6, 28.2, 26.9, 22.7, 14.2.

**N,N'-Dioctyl-1,4,5,8-naphthalenetetracarboxylic 1,8:4,5-diimide (NDI8):** 1,4,5,8-Naphthalenetetracarboxylic dianhydride (1.00 g, 3.7 mmol) and *n*-octylamine (2.50 mL, 15.3 mmol) were dissolved in dimethylformamide (30 mL) and heated to 120 °C overnight. The dark red reaction mixture to room temperature, water (50 mL) was added and the mixture extracted with dichloromethane (3 × 50 mL). The combined organic layers were washed with water (2 × 100 mL), dried over magnesium sulphate, filtered and the solvent evaporated. The red crude solid was then recrystallised from a dichloromethane and methanol mixture, filtered and washed with cold methanol to leave the product as pink needles (1.44 g, 2.9 mmol, 79 %). $^1$H NMR (400 MHz, $CDCl_3$, 25 °C) $\delta$ 8.74 (s, 4H), 4.18 (t, *J* = 7.7 Hz, 4H), 1.78 – 1.69 (m, 4H), 1.45 – 1.39 (m, 4H), 1.38 – 1.33 (m, 4H), 1.32 – 1.23 (m, 12H), 0.87 (t, *J* = 7.1 Hz, 6H). $^{13}$C NMR (175 MHz, $CDCl_3$, 25 °C) $\delta$ 163.0, 131.0, 126.8, 41.1, 31.9, 29.4, 29.3, 28.2, 27.2, 22.8, 14.2.

**N,N'-Didecyl-1,4,5,8-naphthalenetetracarboxylic 1,8:4,5-diimide (NDI10):** 1,4,5,8-Naphthalenetetracarboxylic dianhydride (2.00 g, 7.5 mmol) and *n*-decylamine (6.00 mL, 29.8 mmol) were added to acetic acid (30 mL). The resulting suspension was stirred at 100 °C overnight. After cooling to room temperature, the solids were collected by filtration and washed with cold methanol. The crude product was recrystallised from a mixture of dichloromethane and methanol to yield the title compound as pale pink crystals (3.76 g, 6.9 mmol, 92%). $^1$H NMR (400 MHz, $CDCl_3$, 25 °C) $\delta$ 8.71 (s, 4H), 4.17 (t, *J* = 7.4 Hz, 4H), 1.77 – 1.68 (m, 4H), 1.46 – 1.18 (m, 28H), 0.86 (t, *J* = 6.9 Hz, 6H). $^{13}$C NMR (100 MHz, $CDCl_3$, 25 °C) $\delta$ 162.9, 131.0, 126.8, 126.8, 41.1, 32.0, 29.7, 29.7, 29.5, 29.4, 28.2, 27.2, 22.8, 14.2.

**(c) X-ray powder diffraction (XRPD) characterization.**

Gently ground powders of compounds NDI4, NDI6, NDI8 and NDI10, synthesized as described above, were deposited in the hollow of a zero-background silicon sample holder, 0.2 mm deep (supplied by Assing spa, Monterotondo, Italy). Diffraction experiments were performed on a vertical-scan Bruker AXS D8 Advance diffractometer in θ:θ mode, equipped with a linear position-sensitive Lynxeye detector, primary beam Soller slits, and Ni-filtered Cu-K$\alpha$ radiation ($\lambda$ = 1.5418 Å).

**(d) Thin film preparation**

All films were prepared under the following conditions: spin-coated on 300nm thick $SiO_2$/Si substrate from NDIx chlorobenzene solution (5 mg/mL) at 800 rpm for 3 seconds, followed by 2000 rpm for 20 seconds. Afterwards, they were dried in air at 70 °C for 15 minutes.

**(e) X-ray diffraction characterization of thin films**

X-Ray Diffraction (XRD) measurements were performed in specular geometry using a SmartLab-Rigaku diffractometer equipped with a rotating anode (Cu-K$\alpha_1$, $\lambda$ = 1.5406 Å), a parabolic mirror to collimate the incident beam and a series of variable slits (placed before and after the sample position) to reach an acceptance of 0.03°. Grazing Incidence X-Ray Diffraction (GIXRD) measurements were performed at the XRD1 beamline of ELETTRA synchrotron facility (Trieste, Italy) by using a wavelength of 1.00 Å and an incident angle of 0.1°. A 2D Pilatus was placed normal to the incident beam direction at 350 mm from the sample. Reciprocal space maps and unit cell indexing were calculated from the measured data using the *GIDVis* software.[18] Unit cell parameters were extracted by using a home-made program able to find the set of {hkl} indices which best fit Bragg peak positions.

**(f) Atomic Force Microscopy (AFM)**

Atomic Force Microscopy was performed in semi-contact mode using an NT-MDT Ntegra Prima instrument mounted on a TS-150 isolation table (Table Stable Ltd). Pyramidal etched silicon AFM probes (Agar Scientific) resonating at ~140 kHz were used for the measurements. 20x20 µm topographic images (512x512 points) were recorded at a line acquisition rate of 0.5 Hz.

**(g) Differential scanning calorimetry (DSC)**

Differential scanning calorimetry was performed on a Perkin Elmer DSC 4000 or DSC 8000 instruments using aluminium pans. The samples were weighed in powder form in the DSC pans and crimped with a lid. Each sample was measured in two subsequent heating/cooling cycles, the second cooling trace being only marginally different from the first one. Remarkable differences were instead observed during the two heating processes. A minimum of two scans per sample was performed.

**(h) Variable Temperature XRPD.**

Thermodiffractometric experiments were performed starting from the pristine x$\alpha$ (x = 4,6,8,10) phases. Powdered batches were deposited in the hollow of an aluminium sample holder, assembled by Officina Elettrotecnica di Tenno, Ponte Arche, Italy; diffractograms were acquired in air, in the most significant low-angle 2$\theta$ ranges. Consistently with the measured DSC trace, NDI6 showed the richest polymorphic behaviour; the different experimental sequences and the pertinent results are presented in the Results and Discussion section. NDI4 and NDI10 also showed polymorphic transitions, later discussed. As in powder diffraction experiments, as well as in polarized optical imaging, the samples are in direct contact with the air and some thermal drifts/gradients are present, the most correct phase transition temperatures are taken from the more accurate DSC measurements, performed as illustrated above.

**h) Variable Temperature Optical Microscopy**

Optical micrographs were recorded with a Nikon i-80 microscope equipped with epi-illuminator and cross polarizing lenses (POM). The images were recorded using LU Plan ELWD 20X/0.40 and 50X/0.55 objectives, a commercial CCD (DIGITAL SIGHT DS-2MV) and 500 ms acquisition time. The entire POM setup is described in ref 19. The thermal treatments were performed under the optical microscope using a Linkam TMHS600 heating stage and a TP94 controller ($\Delta T = \pm 0.1$ °C).[20]

**(i) Variable Temperature XRD and GIXRD on Thin Films**

XRD scans were collected in air in real time on a hot plate placed in contact with the sample holder in the goniometer. The temperature was varied from 20 to 100 °C. At each temperature, the sample was aligned and five XRD scans were collected in 30 m in order to follow any possible slow phase transition. When no differences were observed, XRD scans were summed up to increase the signal to noise ratio. GIXRD images were collected in-situ and in real time during thermal annealing by means of a heated nitrogen gas blower installed next to the sample. GIXRD images were recorded for 20 s once temperature reached stability and sample was aligned. Different thermal treatments were carried out, from RT up to 80°C, 100°C and 120°C and reversibility was checked by cooling to RT and repeating the thermal treatment.

**(k) Other Methods**

Solution NMR spectra were recorded using a Bruker Avance III 400 and Neo 700 spectrometer, operating at 400 and 700 MHz, respectively. Chemical shifts are reported in ppm with the residual solvent peak of $CHCl_3$ ($\delta$ = 7.27 ppm, s) as the internal standard. UV-Vis spectra were recorded in chloroform solutions on a Shimadzu UV-2600 spectrophotometer.

## 3. Results and Discussion

**(a) Crystal structures**

X-ray diffraction traces of the 4$\alpha$ and 6$\alpha$ phases matched those found in the CSD database.[21,22] At variance, no structural model was found for 8$\alpha$ and 10$\alpha$, thus requiring a complete *ab-initio* structural solution from powder diffraction data only. Details are provided in the ESI.

Helping the reader Figure 1, which shows the molecular structures and crystal packing of four species (the $\alpha$ crystal phases of NDIx with x = 4,6,8,10, stable at the room temperature, RT), is here anticipated and will be discussed in this and in the following sections.

*Crystal Structure of 8$\alpha$.* Crystals of 8$\alpha$ are triclinic, P-1, with the molecule lying on an inversion center. The *n*-octyl chain conformation is nearly in *all-trans* geometry (maximum deviation *ca.* 12°) with the notable exception of a slight twist at the two terminal torsions, found to approach 140° (Figure 1, left). As powder diffraction on molecular materials of moderate complexity is known to afford approximate geometrical parameters the highest care was taken in assessing the validity of this model, for example by thoroughly exploring the parameter hyperspace and by restraining torsional angles to

more widely accepted values.

As a further confirmation of the occurrence of such an anomaly our variable temperature XRPD measurements, and lattice parameter refinement derived therefrom, provided the clue for such a behavior. Indeed, by heating the sample a very large increase of the c axis from the 22.7 Å at RT to 23.7 Å at 175°C was observed. This accounted for a 4.2% relative change for a giant linear thermal expansion coefficient of 280 $MK^{-1}$ as expected for the complete stretching, and perhaps dynamic rotation, of the entire *n*-octyl residue. A CSD search of *n*-octyl analogues in purely organic molecules indicated that torsion angles in the outermost region are possible, though rare.[23,24] Additionally, we found that this transformation is continuous and fully reversible, restoring identical XRPD traces upon cooling.

*Crystal data for 8a (NDI8 a-phase)*: $C_{30}H_{38}N_2O_4$, fw = 490.64 g $mol^{-1}$, triclinic P-1, a = 4.7814(2) , b = 6.5335(3) , c = 22.7590(9) Å, $\alpha$ = 87.874(2), $\beta$ = 88.991(5), $\gamma$ = 75.754(3) °, V = 688.91(5) $Å^3$, Z = 1, $\rho_{calc}$ = 1.183 g $cm^{-3}$, μ(Cu-Kα) = 6.2 $cm^{-1}$, $R_p$ and $R_{wp}$, 0.063 and 0.090 respectively, for 4301 data collected in the 6-92° 2θ range. $R_{Bragg}$ = 0.054.

*Crystal Structure of 10*$\alpha$. In the RT $\alpha$-form, crystals of NDI10 are triclinic, P-1, with the molecule lying on an inversion center. The *n*-decyl chain conformation is *all-trans* geometry, with most torsion angles falling within 3° from the ideal 180° value and a single, slightly bent, dihedral angle ca. 167.8° (Figure 1). This observation is in line with the structures reported for NDI12 and NDI14 (on single crystal data), where crystal packing efficiency forces long aliphatic chains to pack side-by-side in the fully stretched conformation. This is similar to what was observed for monoclinic and orthorhombic high-density polyethylene. At variance shorter chains (up to *n*-hexyl), where crystal packing is only marginally dictated by aliphatic $CH_2 \cdots CH_2$ interactions, show markedly bent residues and none in *all-trans* conformation.

*Crystal data for 10*$\alpha$ *(NDI10* $\alpha$*-phase):* $C_{34}H_{46}N_2O_4$, fw = 546.64 g $mol^{-1}$, triclinic P-1, a = 4.7502(3) , b = 6.5503(5) , c = 26.9707(7) Å, $\alpha$ = 94.360(4), $\beta$ = 95.183(6), $\gamma$ = 104.428(7)°, V = 769.95(9) $Å^3$, Z = 1, $\rho_{calc}$ = 1.179 g $cm^{-3}$, μ(Cu-Kα) = 6.1 $cm^{-1}$, $R_p$ and $R_{wp}$, 0.061 and 0.087 respectively, for 4301 data collected in the 6-92° 2θ range. $R_{Bragg}$ = 0.030.

**(b) Comparative Crystal Structure Analysis**

The crystal structures of the members of the NDIx (x = 1-14) series, including the newly determined models for NDI8 (8$\alpha$) and NDI10 (10$\alpha$), are here compared. Table 1 synoptically collects the most relevant features, with the notable exception of the NDI3 crystal phase, the only one not showing the parallel stacking of the NDI cores shared by all other crystal structures.

Significantly, the molar volume, $V/Z_{298}$, increases with a strong linearity with the length of the alkyl chain ($R^2$ = 0.998, as in Figure 2a) expanding by *ca*. 25.0 $Å^3$ when a methylene group is added**.** Moreover, for all compounds, the $\pi$–$\pi$ distance attains the same value of *ca.* 3.4 Å.

Beyond helping the accurate prediction of the density of the missing members (*even by extrapolation*), this comparison shows that the packing efficiency of these materials is similar . The intermolecular attraction of the $\pi$-$\pi$ (for the NDI cores) or van der Waals (in their periphery) type are quite comparable, even if in some cases the *all-trans* configuration of the *n*-alkyls is not present in the solid phases. The interplanar ($\pi$-$\pi$) distance of 3.37 ± 0.03 Å indicates that the NDI cores approach as graphitic carbon does (3.35 Å), despite the absence of fully eclipsed C/N atoms and the intrinsic smaller size of N atoms. Despite similarities, two slightly different groups of stacking modes can be envisaged by plotting their position in the $\chi,\psi$ space (defined in Figure 5). Those clustering near $\beta$ = 53° (upper left corner) belong to the n>7 class, where fully stretched alkyls are present, while the n ≤ 6 phases (bottom right) contain, at RT, significantly folded alkyl residues.

A similiar analysis was reported for bithiazoles and pentacenes, where an alternative description of “pitch and roll” angles (P,R) was used to tentatively correlate the charge transport properties with the geometrical parameters of the $\pi$–$\pi$ stacking.[25] Using the same approach, we obtain P = 40.1° and R = 26.7° for the n>7 class, and P = 48.6° and R = 19.3° for the n ≤ 6 one. As large roll angle inclinations (above 45°) essentially destroy superposition between the $\pi$-orbitals of adjacent molecules, the limited R values determined here should provide effective overlap.

Unexpectedly, the colours of the $\alpha$ phases of the four examined compounds are quite different being yellow (4$\alpha$), pink (6$\alpha$), orange (8$\alpha$) and white (10$\alpha$), see ESI. These visual observations do not correlate with the geometrical parameters reported in Table 1, where the overlap of all the NDI core is very close, but they are likely affected by the grain size.[26] Indeed, the crystallite grain size for ND10 is much smaller than that of the other compounds, providing a whitening of the pristine hue expected for a massive (single) crystal.

Figure 2b shows the smooth and regular trend of the melting points of the NDIx (x=1-14) series taken from the literature or measured by us. This behaviour indicates that increasing the molecular weight and complexity causes the melting points to unexpectedly become lower for longer alkyl chains, despite the NDI core interaction being fairly similar. A comparable decrease of clearing points of substituted metal phthalocyanines, with large *n*-alkyls in the molecular periphery, was recently reported.[27] While these trends are in clear disagreement with the melting point sequence of *n*-paraffins when increasing the molecular complexity,[28] we tentatively put forward the following interpretation:

*a)* The extremely linear increase of the molar volumes (Figure 2a), which are expanded by *ca*. 49.0 $Å^3$ by the presence of two additional methylene groups, implies a near constancy of the van der Waals interactions between the *n*-alkyls. This is regardless of their conformation (values of 47.8 and 49.5 $Å^3$ are nicely predicted by Hoffmann[29] and Mighell[30] models respectively). The fusion enthalpy increment upon increasing *n*, $d\Delta H_{fus}/dn$, can thus likely be considered fairly constant (i.e. $d\Delta H_{fus}/dn>0$).

*b)* Melting point temperatures ($T_{fus}$'s), if equilibrium conditions are assumed, can be written as $T_{fus} = \Delta H_{fus}/\Delta S_{fus}$.

c) As both $\Delta H_{fus}$ and $\Delta S_{fus}$ are positive values, combining the above considerations with the experimental $dT_{fus}/dn<0$ trend

(as per Figure 2b), implies that $d(1/\Delta S_{fus})/dn<0$ or equivalentlythat $d\Delta S_{fus}/dn>0$.

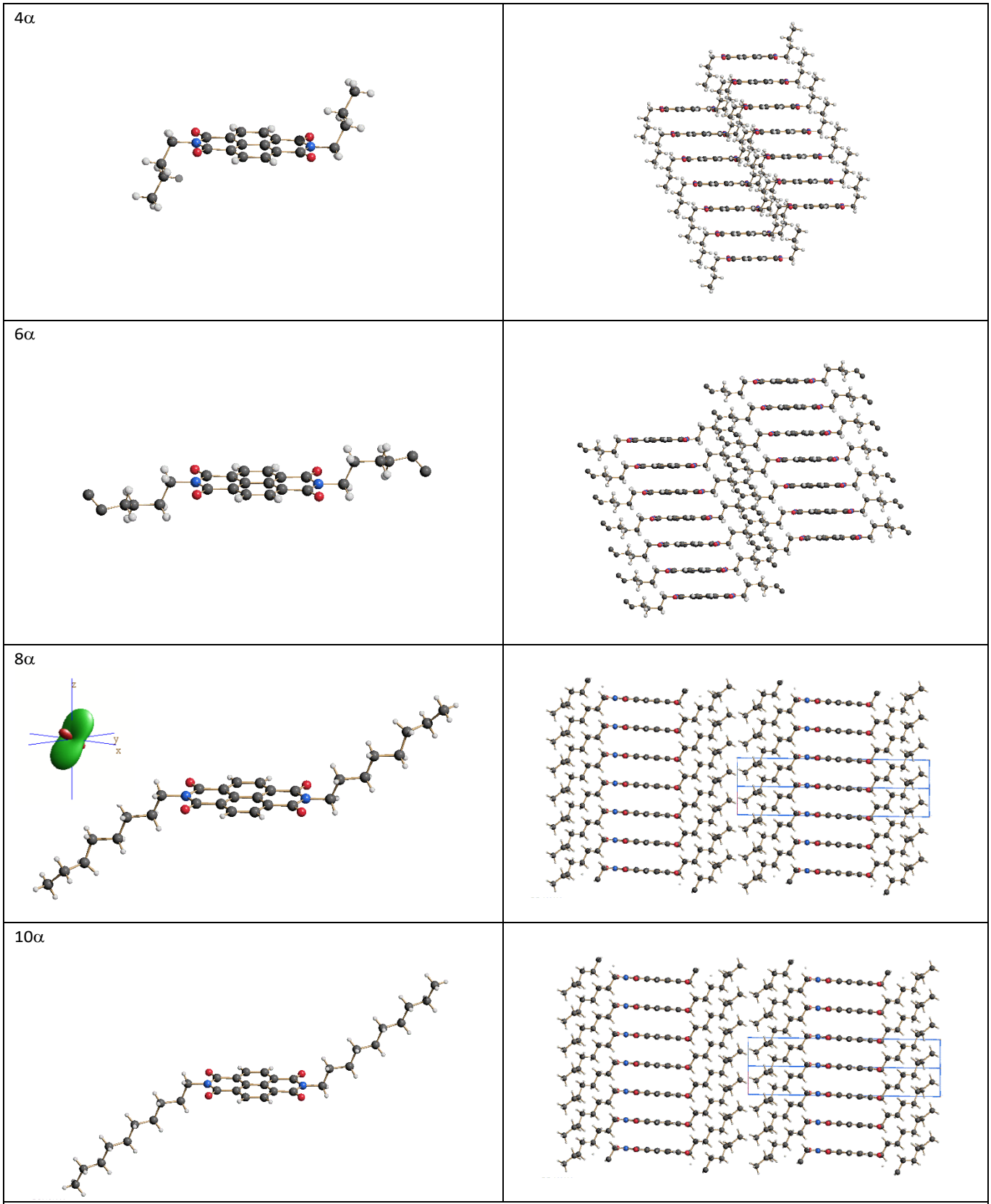


Fig 1 Left: sketches of the molecular geometry of 4α[13b], 6α,[31] 8α and 10α (top to bottom). Color codes: C (grey), N (blue), O (red), H (white). Drawn by SCHAKAL.[32] Due to some alkyl chain disordering in 6α, some of the alkyl H atoms have not been inserted. The inset in the panel of 8α shows the highly anisotropic shape drawn from the thermal expansion coefficient for NDI8, heated from RT to 175°C. Right: sketches of the corresponding molecular packing.

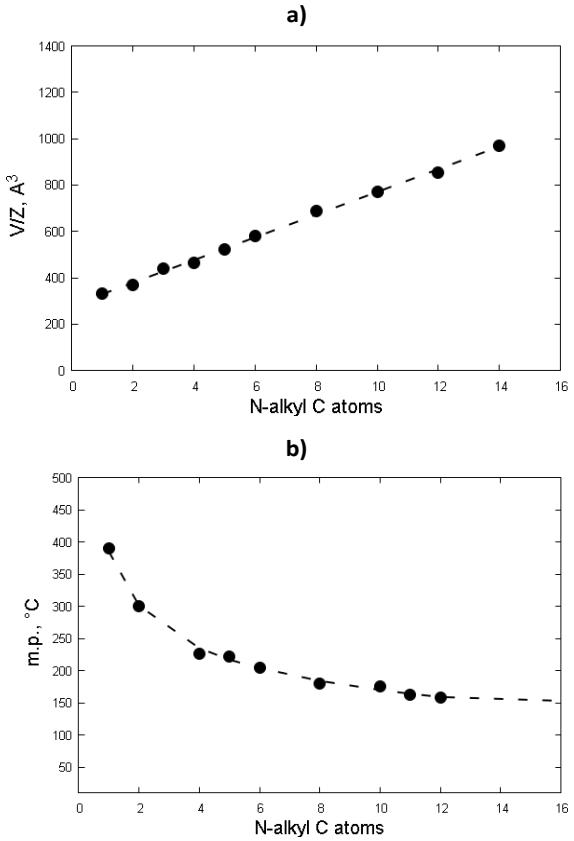


Fig. 2 a) The regular change of the temperature-corrected $V/Z_{298}$ values for the entire NDIx series (x =1-14). b) melting points of the NDIx materials *vs* n-alkyl C atoms. Data were fit by a phenomenological exponential law:

$$m.p.(NDIn) = 163.42 + 321.35\ e^{-0.383n}.$$

For $n \rightarrow \infty$, m.p. should reach an asymptotic value close to 163°C, while ultra-high molecular weight polyethylene melts at 147°C.[33] The slight discrepancy can be easily interpreted by the use of an arbitrary functional dependence (an exponential law), not fully valid outside the range of experimentally available m.p. values.

This analysis suggests that the major factor influencing the steady decrease of the melting point values, upon increasing the chain length, must be attributed to progressively increasing fusion entropy changes. Whether this is due to a larger conformational freedom of the larger alkyl derivatives in the liquids or to their more ordered chain arrangement in the solids cannot be derived from the presently available data.

**(c) Structure of the Films**

The 2D-GIXRD images of all the spin coated films of the NDIx series (x = 4,6,8, 0, Figures 3a-c, 4a and S8a-d) exhibit several intense Bragg spots having small arc shape and a perfect symmetry with respect to the central vertical line. These features indicate the occurrence of films possessing a high degree of crystalline order and texturing, with grains oriented along one specific direction with respect to the normal to the substrate surface.

For NDI4, NDI8, and NDI10 films, all the reflections could be indexed by using the crystallographic structure of the RT-stable $\alpha$-phase of the bulk and, assuming the (001) texturing, are confirmed by the XRD specular scans (Figures 4b and S7e-h), where only *00l* reflections are observed. The experimental reciprocal space images are in good agreement for both position and intensity of the diffracted spots, with the 2D-GIXRD simulations[34] for polycrystalline films composed of molecules highly oriented with the ab plane parallel to the substrate surface (Figures 3d-f). These results allowed us to establish the orientation of the molecular packing in the film system, schematically reported in Figures 3g-i.

AFM topographic images of NDI8 show continuous films with a terrace structure and steps corresponding to molecular monolayers of the NDI8 molecule (Figure S7). Further analysis reveals an average height of these terraces of 2.20 nm ± 0.05 nm, confirming that the molecules pack edge-on to the substrate.

More interestingly, the spin coated film of the NDI6 molecules differs from the others because of the coexistence of two polymorphs: a minor portion of the known phase,[31] here labelled 6$\alpha$, and a larger portion of a still unknown crystalline form, hereafter referred to as 6$\beta$ phase. The experimental 2D-GIXRD image is shown in Figure 4a. The specular diffraction patterns (Figure 4b) indicates that both phases are strongly textured with their (00l) planes lying parallel to the surface (as illustrated for the $\alpha$ phase in Figure 4c).

The broadening of the GIXRD Bragg spots induced by the beam footprint did not allow to solve the 6$\beta$ phase crystal structure. A possible set of unit cell parameters of the 6$\beta$ phase,however, was extracted from Bragg positions in the 2D-GIXRD image ($q_{xy}$ and $q_z$ values of Figure 4a) and in the specular scan[35] (Figure 4b). The resulting cell parameters are: a = 39.50(5) Å, b = 4.71(2) Å, c = 22.60(5) Å, $\alpha$ = 90.0(1)°, $\beta$ = 52.8(1)°, and $\gamma$ = 90.0(1)°. The corresponding cell parameters in conventional setting[36] are a = 22.60 Å, b = 4.71 Å, c = 31.489 Å, $\alpha$ = 90.0°, $\beta$ = 92.33°, and $\gamma$ = 90.0°. Figure S9 shows that the calculated positions of Bragg peaks from this monoclinic setting are in good agreement with the experimental data.

Surprisingly, the $\beta$ phase is characterized by one very long periodicity (ca. 3 nm). These observations will be further substantiated by the full variable-temperature XRPD analysis reported in a following section.

**(e) Thermal properties of the NDIx materials (x = 4, 6, 8 and 10)**

The raw materials obtained after precipitation from their $CH_2Cl_2/CH_3OH$ solutions were characterized by DSC, thermodiffractometry and variable temperature polarized optical microscopy (POM). DSC curves recorded during the 1st heating and cooling cycles and a subsequent 2nd heating cycle (Figure 6) show for all the compounds, but NDI8, a large number of thermal events. These were also followed, from a structural point of view, by separated XRPD and POM imaging. The data extracted from DSC traces are reported in Table 2.

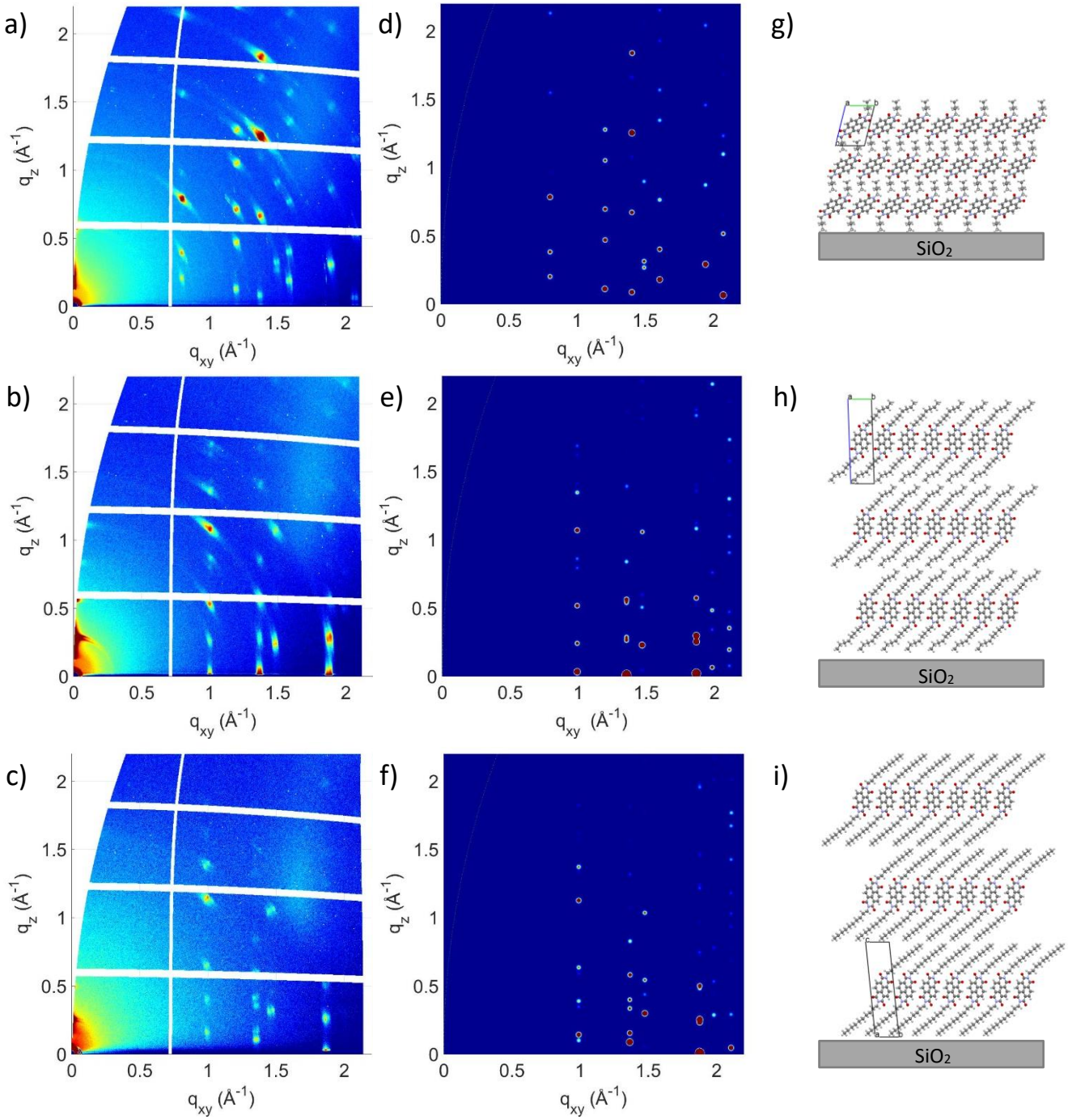


Fig. 3 Experimental and simulated 2D-GIXRD images of NDI4 (a, d), NDI8 (b, e) and NDI10 (c, f) films, toghether with a sketch of their molecular arrangment ($\alpha$ phases; g, h, i).

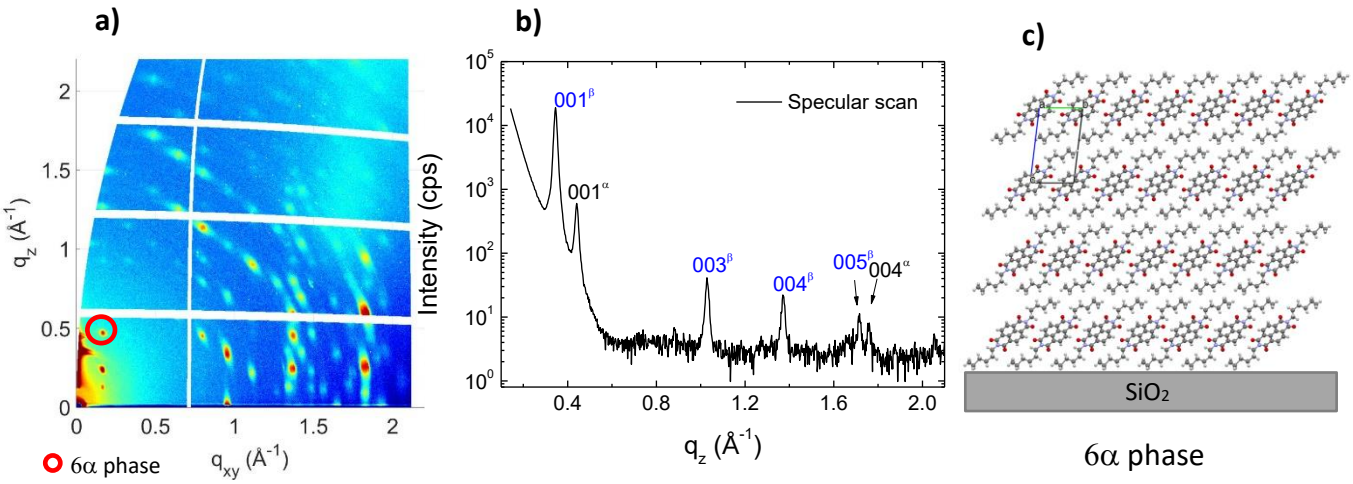


Fig. 4 a) Experimental 2D-GIXD image and b) specular scan of the NDI6 film; c) sketch of molecular arrangement of 6α phase.

**Table 1** Synoptic collection of structural properties and melting points (m.p.) of the known NDIx materials (x = 1-14), with formulae $C_{14+2x}H_{6+4x}N_2O_4$. SG is space group, T is measurement temperature of diffraction data, $V/Z_{298}$ is the molar volume, corrected from the actual measured value $V/Z_T$ using the formula: $V/Z_{298} = V/Z_T\,[1+3\kappa(298-T)]$, with $\kappa = 10^{-4}$ K$^{-1}$; m.p. is the normal melting point; χ, ψ and φ are the angles of the direction cosines of the stacking vector (SV) [Figure 3a] and π–π is the interplanar distance between two parallelly stacked NDI cores.

| Compound | CSD Code | SG | T (K) | $V/Z_{298}$ (Å$^3$) | m.p., °C | χ (°) | ψ (°) | φ (°) | π–π (Å) |
|---|---|---|---|---|---|---|---|---|---|
| NDI1 | DAHMUZ | $P2_1/c$ | 100 | 334 | 390 | 79.02 | 48.32 | 43.77 | 3.403 |
| NDI2 | BIYRIM | $P2_1/c$ | 100 | 368 | 300 | 77.98 | 44.60 | 47.89 | 3.328 |
| NDI3 | DAHLOQ | Pbca | 100 | 439 | | | | | |
| NDI4 | UNANAZ | P-1 | 100 | 465 | 233 | 74.38 | 43.46 | 50.73 | 3.371 |
| NDI5 | RAGJIT | $P2_1/n$ | 123 | 524 | 222 | 80.53 | 42.18 | 49.38 | 3.330 |
| NDI6 | KEKJIU01 | P-1 | 293 | 579 | 204 | 76.23 | 46.44 | 46.81 | 3.347 |
| NDI7 | unknown | | | | | | | | |
| NDI8 | **this work** | P-1 | 298 | 689 | 186 | 68.73 | 53.37 | 44.29 | 3.422 |
| NDI9 | unknown | | | | | | | | |
| NDI10 | **this work** | P-1 | 298 | 770 | 183 | 68.41 | 53.20 | 44.67 | 3.378 |
| NDI11 | unknown | | | | 163 | | | | |
| NDI12 | UNANED | P-1 | 113 | 855 | 158 | 70.10 | 52.70 | 44.03 | 3.376 |
| NDI13 | unknown | | | | | | | | |
| NDI14 | ISELIB | P-1 | 120 | 970 | | 70.70 | 52.71 | 43.64 | 3.415 |

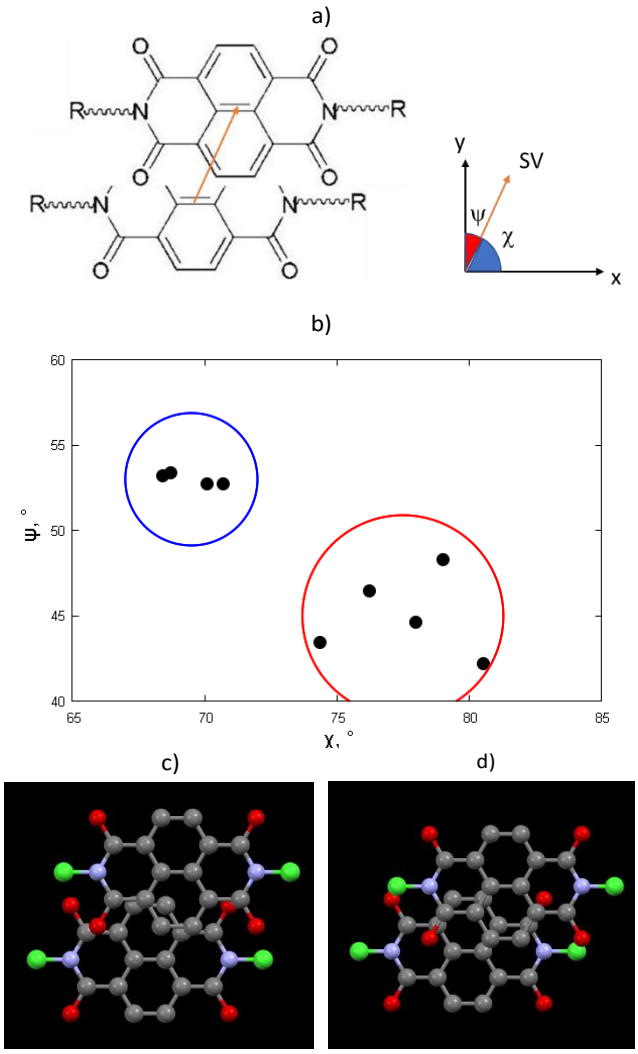


Fig. 5 a) Schematic definition of the stacking vector (SV) between two parallel NDI cores. Z is normal to the xy plane, and the SV must be taken *in 3D space*. Cos$\chi$, cos$\psi$ and cos$\varphi$ are the direction cosines of the stacking vector, while the interplanar distance ($\pi$–$\pi$) is, simply, the *z*-coordinate of the SV. b) Clustering (in the blue and red circles) of the different $\chi/\psi$ values for two markedly different stacking modes. The upper dots, for which $\psi \approx 53°$, belong to the long chain derivatives (x = 8,10,12,14). In the red circle, short chain derivatives (x = 1,2,4,5,6). Note that, since $\cos^2\chi+\cos^2\psi+\cos^2\varphi=1$, any other section of the $\chi,\psi,\varphi$ 3D space would have provided the same information. c,d) Sketches of the two slightly different $\pi$–$\pi$ overlaps, drawn for c ): $\chi = 69°$ and $\psi = 53°$ (blue circle in b) and d): for $\chi = 77°$ and $\psi = 43°$ (red circle in b).

*Thermal characterization of NDI4.* The thermal behavior of the NDI4 species (of known crystal structure[21]) is somewhat complex. Indeed upon heating (red curve in Figure 6) two endothermic events are observed at 123°C and 225°C, both associated (by XRPD) to polymorphic transitions, while melting occurs at 233°C. The presence of a tiny peak between the two polymorphic transitions suggests an additional phase transformation. Upon cooling, the melt crytallizes at 227°C (with a small hysteresis) and a solid-solid phase transition is observed at ca. 164°C. The second heating cycle replicates the first one except for a slight shift at a lower temperature of the peak corresponding to the first transition.

Insights on the nature of these thermally induced transformations can be obtained by studying the evolution of the XRD powder patterns during the first heating and subsequent cooling process, reported in Figure 7. The RT 4$\alpha$ phase shows, upon heating, a polymorphic transition at ca. 123°C . However the sudden appearance of many sharp Bragg peaks, just above this transformation temperature, suggests the coexistence of different polymorphs (here named 4$\beta$ and 4$\gamma$). By increasing the temperature, a progressive unbalancing toward the 4$\gamma$-phase is observed.

The presence of low-angle peaks (down to 4.3° 2$\theta$) shows that the 4$\beta$ polymorph contains an asymmetric unit manifestly larger than that observed in the 4$\alpha$ phase, where Z' = 0.5. The unit cell of the 4$\gamma$-phase was determined by synchrotron X-ray data collected at 200 °C, and shown to be triclinic with a = 9.05, b = 11.26, c = 16.14 Å, $\alpha$ = 103.2, $\beta$ = 93.4, $\gamma$ = 72.7°, V = 1527 Å$^3$, Z = 3, Z'=1.5, V/Z =309 Å$^3$, $\rho_{calc}$ = 1.234 g cm$^{-3}$ ($\rho_{calc}$ = 1.43 g cm$^{-3}$, for 4$\alpha$), and *d(001)* = 15.7 Å (GOF = 36.9). However, owing to the structural complexity, the structure of 4$\gamma$ was not further characterized. The transition detected by DSC just above 225°C, occurring a few degrees before melting, was not caught by thermodiffractometry.

Cooling from the melt enabled the formation and stabilization of a liquid crystal (LC) phase, characterized by a single set of harmonics (with *d* = 15.4 Å at 240°C) and eventually turning (in the XRD chamber, near 120°C) into a $\gamma$-rich (4$\beta$,4$\gamma$) mixture. Specifically, XRD indicates that the RT 4$\alpha$ phase could be restored only after a few days with some minor contamination of the high-temperature phase(s).

The transformation of the 4$\alpha$-phase into more than one polymorph upon heating is confirmed by the evolution of POM images. Together with the first phase transition (4$\alpha \rightarrow$ 4$\beta$,4$\gamma$ phases), identified by changes in shape and movements of a few crystallites (Figures 8a-b), the complete 4$\beta \rightarrow$ 4$\gamma$ transition (Figure 8c) is detected at ca. 200°C by contrast image changes. Slightly before melting (i.e. at 240°C, offset from the DSC value by the unavoidable presence of a thermal gradient), a transient LC phase is observed, easily associated to the pre-melting peak observed by DSC.

Interestingly, upon cooling, the melt forms a LC phase with a slight hysteresis (Figure 9a). The LC to (4$\beta$+4$\gamma$) mixture is identified by faint contrast changes within a few domains appearing at 160°C (Figure 9b); such changes progressively intensify by further cooling down to 135°C (Figure 9c). Our observations are in agreement with the occurrence of two exothermic events observed upon cooling near 226°C and 160°C, observed in our DSC traces and already reported in literature, but not interpreted.[21]

Only well below 70°C cracks in the crystals form (Figures 9d,e); attributed through diffraction to the incipient and partial formation of the original 4$\alpha$-phase (longer times are found to be necessary in the XRD diffractomer setup).

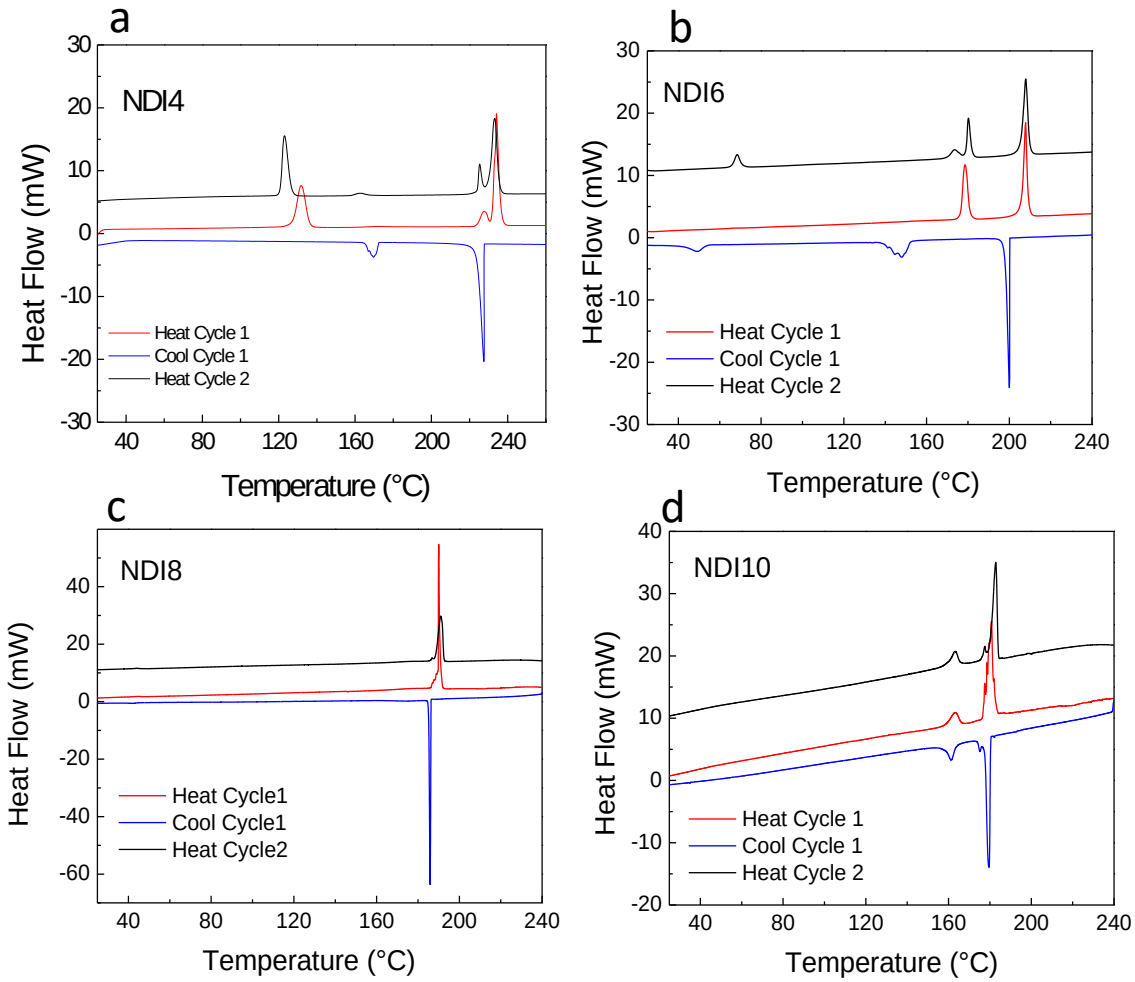


Fig. 6 DSC traces measured on the pristine NDIx (x = 4, 6, 8 and 10) powders, upon heating, subsequent cooling and second heating (red, blue and black traces, respectively).

**Table 2** Summary of the transition temperatures (°C) and enthapies (kJ mol$^{-1}$) for the NDIx (x = 4, 6, 8 and 10) species. Italicized items indicate broad, and difficult to detect, thermal events. Only the second heating and cooling cycle values are here reported. DSC data for the first heating and cooling cycle are supplied in the ESI.

| | NDI4 on heating | NDI4 on cooling | NDI6 on heating | NDI6 on cooling | NDI8 on heating | NDI8 on cooling | NDI10 on heating | NDI10 on cooling |
|---|---|---|---|---|---|---|---|---|
| T | 123.0<br>4α → 4β,4γ<br>(coexisting) | *Very slow transformation to 4α* | 68.3<br>6β → 6γ | 47.6<br>6γ → 6α,6β | | | 163.2<br>10α → 10β | 160.3<br>10β → 10α |
| ΔH | 17.6 | *n.a.* | 4.5 | −3.7 | | | 8.3 | −7.2 |
| T | 162.8<br>4β → 4γ | 155.2<br>LC → 4γ,4β | 173.5<br>6α → 6γ | | | | *178*<br>*10β → 10γ,* | *172*<br>*10γ → 10β* |
| ΔH | 1.1 | −2.3 | 2.3 | | | | *n.a.* | *n.a.* |
| T | 225.2<br>4γ → LC | 164.4<br>LC → 4γ,4β | 180.2<br>6γ → 6δ | 146.7<br>6δ → 6γ | | | | |
| ΔH | 3.9 | −1.4 | 7.1 | −13.0 | | | | |
| T | 233.2<br>melting | 226.8<br>melt→LC | 208.0<br>melting | 199.8<br>melt→6$\delta$ | 192.7<br>melting | 186.3<br>crystallization | 182.8<br>melting | 178.2<br>melt→10$\gamma$ |
| ΔH | 18.8 | −22.2 | 22.6 | −21.5 | 30.5 | −30.8 | 31.4 | −29.2 |
| $\Delta H_{\alpha-melt}$ | 41.4 | n.a. | 36.5 | −38.2 | 30.5 | −30.8 | n.a. | n.a. |

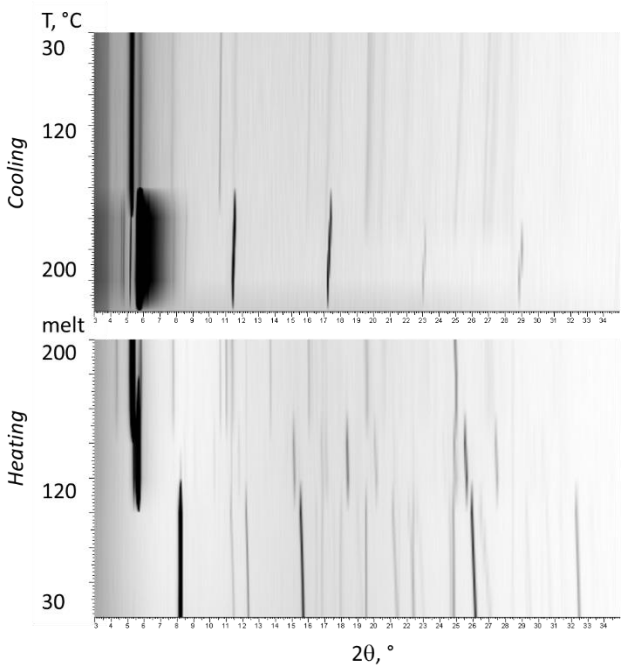


Fig. 7 2D thermodiffractometric plots of NDI4 recorded during heating, and upon cooling from the melt. 2θ-scale: 3-35°.

*Thermal characterization of NDI6.* The very complex thermal behavior of NDI6 also requires a dedicated analysis. The DSC thermograms (Figure 6b) show that the two endothermic events occuring during the first heating cycle (red trace) are not reversibly reproduced upon cooling (blue trace), where an additional transition is observed at ca. 50°C. Moreover, the second heating cycle differs remarkably from the original one. The understanding of such complex thermal behaviour was indeed possible thanks to a combined analysis of powder thermodiffractometry, the results of which are summarized hereafter and depicted in Figure 10, andby POM shown in Figure 11.

At RT the starting powders contain only the pure 6α phase which completely transforms into other species near 180°C. XRPD showed that two distinct polymorphs, 6γ and 6δ, are formed the latter melting at *ca*. 208°C. Separation of two successive events (6α → 6γ and 6γ → 6δ) in the DSC measurements was only possible in the second heating cycle, the transformations being observed at *ca.* 173°C and 180°C respectively. Upon cooling from the melt crystallization of the 6δ phase at ca. 200°C is observed, further transforming at *ca.* 147°C, to 6γ. Only below 50°C does 6γ start to slowly restore 6α together with a larger amount of a new phase, stable at RT, labeled 6β. A mixture of 6α and 6β is then typically formed after the first heating-cooling cycle. The presence of an additional crystal phase, 6β, in the RT material thus explains the new endothermic peak observed at 68°C in the DSC trace of the second heating (Figure 6b, black curve).

The collected XRD data for the 6β, 6γ and 6γ phases, though not possessing enough quality for a full structural determination, provided the lattice parameters reported in Table 3. They showed a remarkable desymmetrization process on raising the temperature in the 6α,γ,δ sequence (see Z' values) and very distinct molecular symmetries for the two RT stable 6α,β phases (of comparable crystal density). This anomaly is later commented in a dedicated section. A tentative model for the crystal structure of the high-temperature 6γ phase is presented in the SI.

**Table 3** Lattice parameters (Å,°) of the four crystal polymorphs of NDI6.

| Phase | S.G. | a | b | c | α | β | γ | Z | Z' | V/Z, Å³ |
|---|---|---|---|---|---|---|---|---|---|---|
| 6α | P-1 | 4.89 | 8.26 | 14.50 | 96.3 | 98.0 | 93.6 | 1 | 0.5 | 575 |
| 6β | P... | 22.84 | 4.85 | 32.06 | 90 | 91.9 | 90 | 6 | 1.5 | 592 |
| 6γ | P-1 | 4.89 | 6.50 | 20.05 | 91.2 | 95.6 | 104.219 | 1 | 0.5 | 616 |
| 6δ[a] | $P112_1/b$ | 8.83 | 8.03 | 37.96 | 90 | 90 | 95.2 | 4 | 1 | 671 |

[a] We chose the non standard S.G. setting for 6δ to keep **c** as the longest cell axis (along which the NDI6 molecules tend to align).

Interestingly only POM images could catch the formation of a LC phase at high temperature. Indeed during the first heating process the first phase transitions (α→γ,δ ), complete at 180°C, is identified by the bending and change of contrast of many crystals (Figure 11a-b). At 211°C, we observed a dramatic change of the crystal shape, with the material behaving as a liquid while preserving optical brightness (Figure 11c). Melting to an isotropic liquid was observed just one degree above, at 212 °C (Figure 11d). POM images recorded during the first cooling process (Figure S10) confirm the polymorph transitions already discussed.

Noteworthyis the 6β phase observed in the powder at RT after the first thermal treatment corresponds to the majority phase observed in the spin-coated thin films (described above in section c, and shown in Figure 4), as demostrated by the simulated 2D-GIXRD (Figure S9). Interestingly in the drop casted films the α phase prevails (Figure S10), suggesting that 6β and 6α are the kinetically and thermodynamically favoured phases respectively.

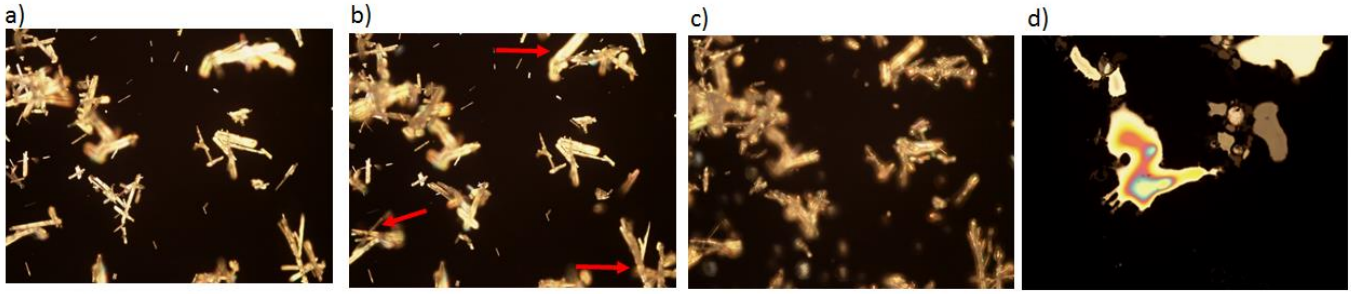

Fig. 8 POM images of NDI4 recorded during a first heating cycle at a) 25, b)135, c) 200 and d) 240 °C.

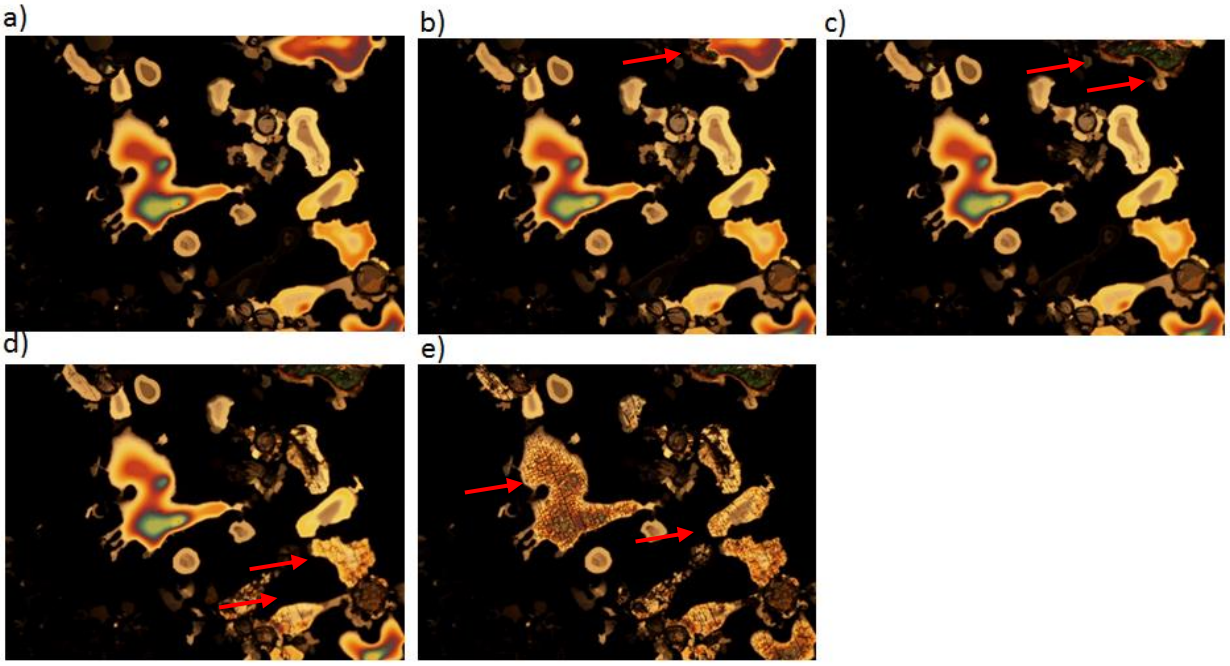


Fig. 9 POM images of NDI4 recorded during cooling from the melt, at a) 230, b) 167, c) 135, d) 65 and e) 45°C.

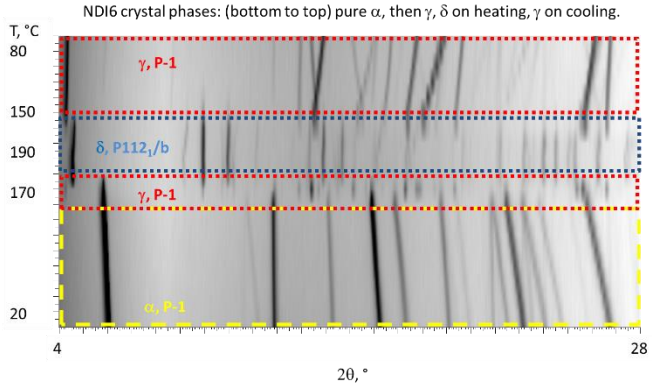


Fig. 10 2D map of XRD patterns of NDI6 powder recorded during thermal treatment (heating and cooling).

We verified the presence/stability of the different NDI6 polymorphs in thin films by recording 2D-GIXRD images, *in-situ*, during heating (from RT up to 120°C) and subsequent cooling (down to RT). A movie is available in ESI (Movie.1) to watch the evolution of the Bragg spots during the thermal annealing. This analysis was carried out only at relatively low temperatures, because beyond 120°C film dewetting prevented further investigation (watch Movie.2 in ESI).

From RT up to 80°C, all 2D-GIXRD images are identical (one for all is shown in Figure 12a). By raising the temperature up to 120°C the 6$\alpha$ phase remains stable whereas 6$\beta$ vanishes and transforms into another polymorph, identified as 6$\gamma$. Indeed, the experimental 2D-GIXRD image measured at 120°C (Figure 12b) can be well reproduced by assuming a (001) textured film with 6$\gamma$ structure (Figure 12c). The 6$\beta \rightarrow$ 6$\gamma$ transition is followed even more clearly observing the change in the out-of plane profiles obtained integrating the 2D-GIXD along the $q_z$ direction (Figure 12f). The 2D-GIXRD image collected at RT after the first thermal cycle (Figure 12d) exhibits the presence of residual 6$\gamma$, together with the 6$\beta$ and 6$\alpha$ phases, indicating that the reverse 6$\gamma \rightarrow$ 6$\beta$ transformation occurs only partially, the transition requiring several days to complete. Specular XRD, OM and AFM measurements performed *in situ*, during the thermal process, confirmed these results (Figures S7, S12, S13, S14 and S15).

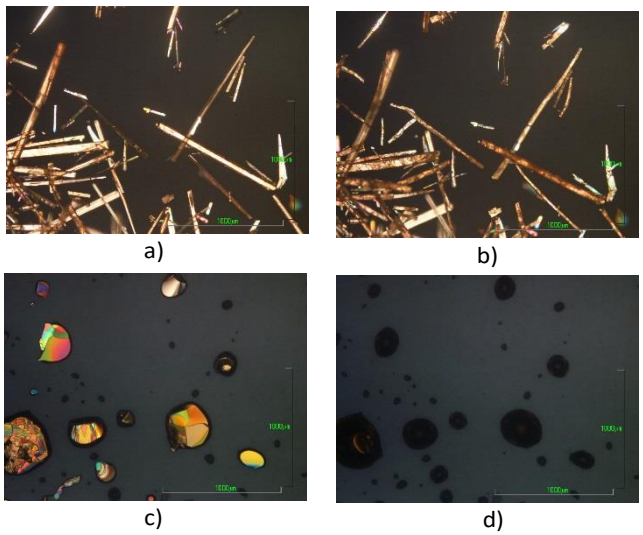

Fig. 11 POM of NDI6 powder recorded during the first heating process: a) 25, b) 180 ($\alpha$ to $\delta$ phase), c) 211 ($\delta$ to LC) and d) 212 °C (melting).

*Thermal characterization of NDI8.* The simplest thermal behaviour was exhibited by NDI8, which only manifested melting of the unique RT 8$\alpha$-phase near 186 °C and recrystallization, upon cooling, at 183 °C with a very minimal hysteresis (Figure 6c).

*Thermal characterization of NDI10.* The largest member of our series, NDI10, shows a completely reversible thermal behavior upon heating and cooling, perfectly reproducible by further thermal cycling. Two main endothermic transitions are observed at 163 and 183°C along with two corresponding exothermic transitions on the cooling cycle.

The origin of these two transitions can be revealed by the analysis of the 2D thermodiffractometric plots (Figure 13). As the platy morphology of the powders enabled a meaningful analysis of the *d*-spacing of the *00l* peaks only, Figure 13a shows the temperature evolution of the *00l* peak positions. Wavy changes due to a progressive unit cell expansion followed by the occurrence of a polymorphic phase transition are observed. Reversibility and reproducibility in a second run were confirmed by subsequent thermal cycling (Figure 13b). Additionally, the DSC curves (Figure 6d) show a reversible event characterized by a tiny peak falling very close to the melting one, escaping the XRPD detection but successfully identified by the contrast change of optical microscopy images, and attributed to the formation of a new (possibly liquid-crystalline) 10$\gamma$ phase.

Conventional POM imaging of the very small crystallites could not directly reveal, upon heating, the ocurrence and nature of any phase transformation. Significant information can be extracted, however, by monitoring the POM images of the continuous film obtained by recrystallization of the melt (Figure 14). Just a few degrees below the onset of recrystallization, at ca. 173°C, a contrast change is observed in very small regions of the film (corresponding to the tiny peak in the DSC curve attributed to the elusive 10$\gamma \rightarrow$ 10$\beta$ transition). This is followed by the more evident contrast change appearing some 10°C lower (and assigned to the 10$\beta \rightarrow$ 10$\alpha$ transition).

**(f) Insurgence of polymorphism: final thoughts.**

Aiming at understanding why the different NDIx (x = 4,6,8 and 10) materials possess such a rich polymorphic versatility, and rather distinct for the different cases, we analysed some of the data presented in previous sections in depth. Together with the optimized crystal structure models (with the caveat that alkyl disorder cannot be easily detected by conventional XRPD structural analysis) our evidence can be summarized as follows.

a) Among the studied materials, only NDI6, in its RT stable 4$\alpha$ form, shows alkyl chains with a remarkable twist from the *all-trans* conformation (the torsion angle on the C9-C10 hinge falling near 67°, typical of a *gauche* conformation).

b) NDI4 and NDI6 belong to a class of stacking vector (SV) orientations different than NDI8 and ND10 (Table 1 and Figure 5b), in which intermolecular $\pi$-$\pi$ interactions likely dominate the overall crystal packing energy in the presence of short(er) *n*-alkyls.

c) Longer alkyl branches, in *all-trans* disposition, likely force through their "polyethylene like" arrangement. The occurrence of SV's, shown in Figure 5b (upper left class), is less widely spread than for shorter branches.

d) NDI8 is thermally silent, while longer chains (as in NDI10) induce the formation of additional thermally induced polymorphic transformations, which differ from lighter NDIx analogues (x = 4 and 6) and are found to be fully reversible.

e) In spin coated films the molecular assembly may be affected by the interaction with the substrate, with crystal nucleation and growth driven by competing kinetic effects. Among the studied materials only in the case of NDI6 the thin film structure differs from the RT bulk phase.

Understanding these bare facts is not easy, nevertheless we tentatively put forward the following interpretation.

Firstly, when shorter alkyl chains are present, the overall crystal packing is mostly governed by molecular core interactions (i.e., $\pi$-$\pi$). This ensures a wider chain flexibility, where *gauche* or other twisted conformations are not detrimental to the formation of alternative polymorphic forms, occasionally coexisting at the same temperature conditions (as found for both NDI4 and NDI6 compounds).

Secondly, the occurrence of the gauche conformation in both *n*-hexyl residues (here, *g,g*) of 6$\alpha$ may explain why a rather complex 6$\beta$-phase (likely with Z'= 1.5) can coexist at RT with 6$\alpha$. A probable interpretation could be that the *g-g* conformation, as well as the *g,a* and *a,a* conformations (*a* stands for *anti*), reasonably exist as local minima of the global *molecular* energy hypersurface. This is in line with the unit cell size and symmetry of the 6$\beta$-phase, as well as with the likely presence of a single *a,a* conformer in the high temperature 6$\gamma$-phase. Indeed, the absence of full reversibility of the pertinent phase transitions may be justified by the rather different crystal complexity in the Z' = 0.5, 1.5 and 0.5 sequence of the 6$\alpha$,$\beta$,$\gamma$ crystal phases detected by XRPD.

Additionally formation of the 6$\delta$ crystal phase (with Z' = 1), apparently breaking the common belief that increasing the temperature causes symmetry enhancement, may be tentatively explained by the occurrence of not fully counterbalancing molecular desymmetrization and crystal symmetry changes (triclinic to monoclinic). All these hypotheses cannot be easily tested due to the coexistence of multiple phases, structure complexity and intrinsic peak broadening.

Differently the reversible 10$\alpha \rightarrow$10$\beta$ transition, occurring near 163°C upon heating, can be interpreted as a formation of a rotator phase. This was already described for longer *n*-alkanes by Hammami et al.[37] Using the $\Delta$T values ($\Delta T = T_{melting} - T_{crystal\text{-}rotator\ phase\ change}$) reported therein, and calibrated *vs.* the number of carbon atoms in the chain, a rough estimate of the $\Delta$T separation for n = 10 gives $\Delta$T = 12°C. This is in line with the temperature difference of the first two endothermic events observed in the DSC traces (the 10$\alpha$ to 10$\beta$ transition and the formation of the 10$\gamma$ - liquid crystalline - phase just before melting).

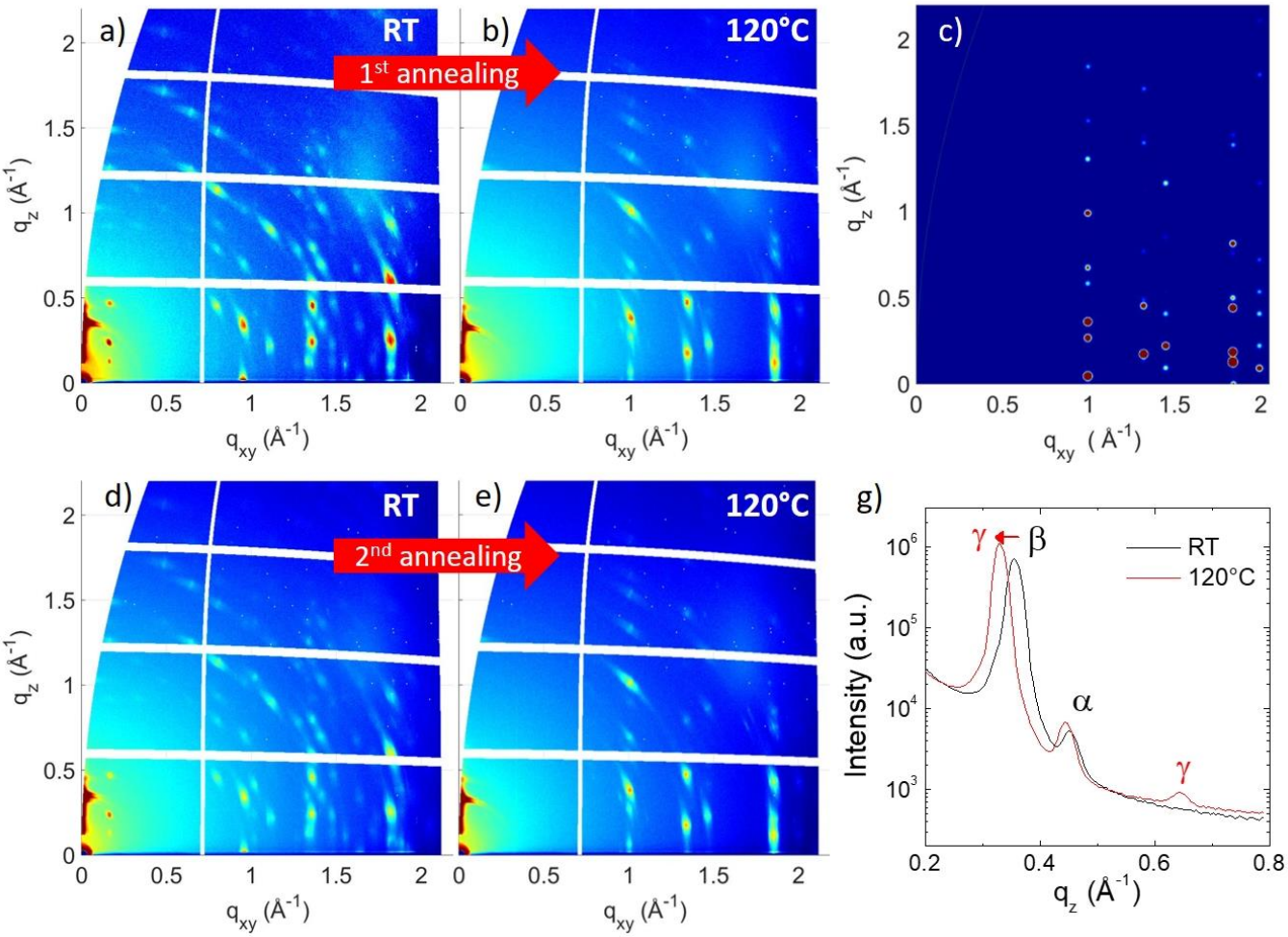


Fig. 12 For NDI6 films experimental 2D-GIXD images a) at RT and b) at 120°C after the 1st heating process; c) simulated image of the 6γ phase; 2D-GIXRD images d) at RT after the 1st cooling process and e) at 120°C after the second heating; f) out-of-plane integration of the a) and b) images in the region depicted by the blue box in a)

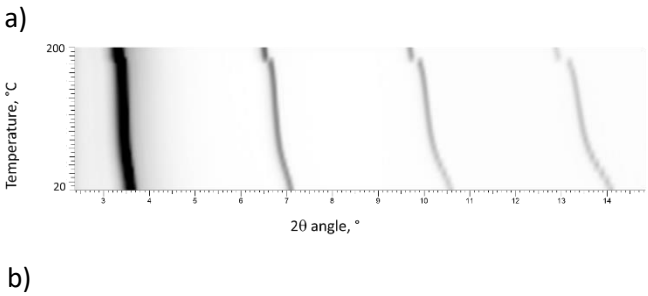


Fig. 13 Top: *00l* peak positions (*l* = 1-4) of heavily oriented powders of the 10α phase, recorded upon heating from 20 to 200°C in 20°C steps. The discontinuity observed above 160°C refers to the 10α → 10β polymorphic transition. Bottom: the sigmoidal variation of the $d_{001}$-spacing (in Å), and the exact superimposition of the values measured in subsequent heating runs. Empty circles: first heating; filled circles: second heating.

More difficult isthe interpretation of the "regular" behavior of 8α, however, insensitive before melting to temperature variations. As NDI4 and NDI6 demonstrated a rich polymorphic behavior induced mostly by the occurrence of alternative (short) chain conformations, and as NDI10 only showed ordered and dynamically disordered *n*-decyl chains, the extended stability of the 8α phase is here tentatively attributed to the presence of a substantially *all-trans* conformation (fairly stabilized over *gauche*-containing conformers). It is also attributed to the lack of rotator phase, typical of solids encompassing longer alkyl chains. If this was true, then 8α is a fortunate case where two competing effects cancel each other.

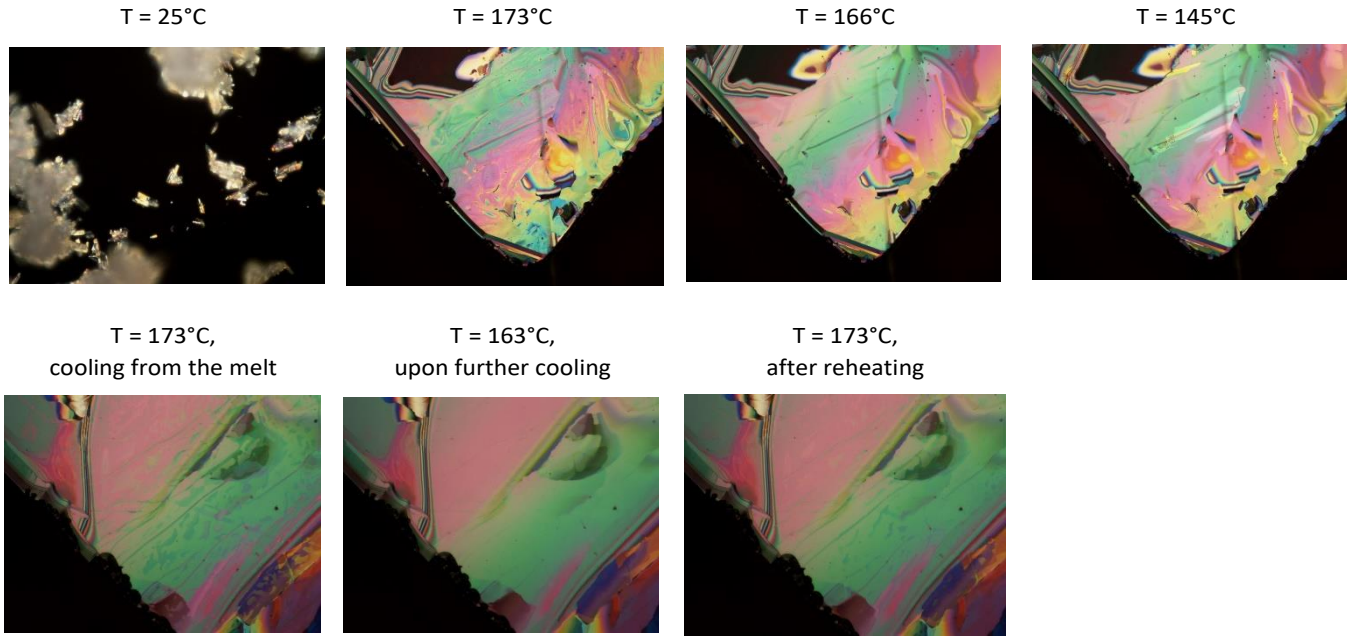


Fig. 14 Top row (left to right): OM images of NDI10 recorded at RT, recrystallized film at 173°C and after cooling down to 166 °C and 145 °C. Bottom row: Contrast change observed upon cooling from 173 °C to 166°C (disappearance of thin black lines) corresponding to the 10$\gamma$ → 10$\beta$ transition, which is reversible upon heating (appearance of thin black lines in the rightmost panel).

## 4. Conclusions

We have studied the versatility of the structural arrangements of naphthalene-diimides bearing linear *n*-alkyl residues (n = 4, 6, 8 and 10). Thermal analyses, supplemented by optical imaging and variable temperature powder diffraction data (including *ab-initio* structure determination) enabled the detection of many polymorphic crystal phases, and in a few cases the formation of transient liquid crystalline mesophases. Reversibility and hysteretic effects were estimated and used to interpret the compositions and texture of these materials when deposited as thin films.

A comparative analysis of their structural properties enabled us to separate the known RT $\alpha$ phases of these materials in two separate classes, characterized by different orbital overlaps, but somewhat surprisingly not manifested by systematic changes in their colours.

As materials of this kind, including PDI derivatives, are widely studied for thin film applications the detailed knowledge of their polymorphism, structures and stability ranges is of utmost importance. Being nearly impossible to structurally characterize them *ab-initio* once deposited, the comprehension of their structural/energetic landscape from polycrystalline powders enabled us to understand the occasional co-presence and mechanism of formation of the different phases under different (powder and film) preparations/treatment conditions. Work can be anticipated to extending this study to analogous materials with larger aromatic cores, or with differently substituted alkyl chains , including polydentate amines in search of structurally and thermally stable crystal phases with enhanced transport properties.

CCDC 1972223-1972224 contain the supplementary crystallographic data for the two crystal structures of the new 8$\alpha$ and 10$\alpha$ compounds, structurally discussed in this paper. These data can be obtained free of charge via www.ccdc.cam.ac.uk/data_request/cif, or by emailing data_ request@ccdc.cam.ac.uk, or by contacting The Cambridge Crystallographic Data Centre, 12 Union Road, Cambridge CB2 1EZ, UK; fax: +44 1223 336033.

## Conflicts of interest

There are no conflicts to declare.

## Acknowledgements

We thank the International Exchanges Scheme (Royal Society) for partial financial support (IE161598). L.C. acknowledges financial support from the EPSRC (EP/N509577/1) and B.S. from the British Council (Grant No. 337067). O.F. thanks the Royal Society for his University Research Fellowship (UF140372), and the EPSRC Centre for Doctoral Training in Plastic Electronic Materials for S.L.'s studentship (EP/L016702/1). This project was partially supported by MIUR (PRIN-2017, Project 2017L8WW48, HY-TEC). We thank Dr. A. Cervellino for assistance during the synchrotron X-measurements at SLS and O.M. Roscioni for software development for GIXRD indexation. We are grateful to Prof. C. Salzmann and Dr. A. Rosu-Finsen for support with the DSC measurements.

## Notes and references


1 M. Caironi and Y.-Y. Noh, *Large Area and Flexible Electronics*, 2015, Wiley VCH, Weinheim (Germany).

2 M.M. Hussain and N. El-Atab*, Handbook of Flexible and Stretchable Electronics*, 2019, CRC Press, Boca Raton, FL (USA).

3 L.A. Francis and K. Iniewski, *Novel Advances in Microsystems Technologies and Their Applications*, 2014, CRC Press, Boca Raton, FL (USA).

4 a) Y. Chen, Y. Zhao and Z. Liang, *Energy Environ. Sci.*, 2015, **8**, 401–422; b) M. Culebras, C. M. Gómez and A. Cantarero, *Materials* 2014, **7**, 6701-6732; c)L.M. Cowen, J. Atoyo, M.J. Carnie, D. Baran and B.C. Schroeder, *ECS J. Solid State Sci. Techn.,* 2017, **6** , N3080-N3088.

5 a) D.M. De Leeuw, M.M. J. Simenon, A.R. Brown and R.E.F. Einerhand, *Synthetic Met.* 1997, *87*, 53-59, b) B.A. Jones, A. Facchetti, M.R. Wasielewski and T.J. Marks, *J. Am. Chem. Soc.* 2007, **129**, 15259-15278.

6 a) Y. Sun, C.-A. Di, W. Xu, and D. Zhu, *Adv. Electron.Mater*.2019, **5**, 1800825, b) J. T. E. Quinn, J. Zhu, X. Li, J. Wang and Y. Li, *J. Mater. Chem. C*, 2017, **5**, 8654—8681.

7 ] a) R. Schmidt, J.H. Oh, Y. S. Sun, M. Deppisch, A.M. Krause, K. Radacki, H. Braunschweig, M. Konemann, P. Erk, Z.A. Bao and F. Würthner, *J. Am. Chem. Soc.* 2009, **131**, 6215-6228. b) R.T. Weitz, K. Amsharov, U. Zschieschang, E.B. Villas, D.K. Goswami, M. Burghard, H. Dosch, M. Jansen, K. Kern and H. Klauk , *J. Am. Chem. Soc.* 2008, **130**, 4637-4645; c) C. Piliego, F. Cordella, D. Jarzab, S. Lu, Z. Chen, A. Facchetti and M.A. Loi , *Appl. Phys. A - Mater.* 2009, **95**, 303-308; d) M.L. Tang, J.H. Oh, A.D. Reichardt, Z.N. Bao, *J. Am. Chem. Soc.* 2009, **131**, 3733-3740; e) J. Rivnay, L. H. Jimison, J. E. Northrup, M. F. Toney, R. Noriega, S. F. Lu, T. J. Marks, A. Facchetti and A. Salleo, *Nature Mater.* 2009, **8**, 952-958; f) L. Ferlauto, F. Liscio, E. Orgiu, N. Masciocchi, A. Guagliardi, F. Biscarini, P. Samorì and S. Milita, *Adv. Funct. Mater.* 2014, **24**, 5503–5510; g) F. Liscio, S. Milita, C. Albonetti, P. D'Angelo, A. Guagliardi, N. Masciocchi, R.G. Della Valle, E. Venuti, A. Brillante and F. Biscarini, *Adv. Funct. Mater.* 2012, **22**, 943–953.

8 C. Li and H. Wonneberger, *Adv. Mater.* 2012, **24**, 613-636.

9 X. Zhan, A. Facchetti, S. Barlow, T. J. Marks, M. A. Ratner, M. R. Wasielewski and S. R. Marder, *Adv. Mater.* 2011, **23**, 268–284

10 M. Al Kobaisi, S.V. Bhosale, K. Latham, A. Raynor and S.V. Bhosale, *Chem. Rev.* 2016, **116**, 11685-11796.

11 a) M.R. Molla and S. Ghosh, *Chem. Eur. J.* 2012, **18**, 1290-1294; b) A. Das and S. Ghosh, *Angew. Chem. Int. Ed. Engl.* 2014, **53**, 1092-1097; c) X. Zhan, A. Facchetti, S. Barlow, T.J. Marks, M.A. Ratner, M.R. Wasielewski and S.R. Marder, *Adv. Mater.* 2011, **23**, 268-284; d) H.E. Katz, J. Johnson, A.J. Lovinger and W. Li, *J. Am. Chem. Soc.* 2000, **122***,* 7787-7792; e) H.E. Katz, A.J. Lovinger, J. Johnson, C. Kloc, T. Siegrist, W. Li, Y.-Y. Lin and A. Dodabalapur, *Nature* 2000, **404**, 478-481.

12 A.O.F. Jones, B. Chattopadhyay, Y.H. Geert, and R. Resel, *Adv. Funct. Mater*., 2016, **26**, 2233–2255.

13 a) M. Dharmarwardana, R.P. Welch, S. Kwon, V.K. Nguyen, G.T. McCandless, M.A. Omary and J.J. Gassensmith, *Chem. Commun.,* 2017, **53**, 9890-9893; b) P.M. Alvey, J.J. Reczek, V. Lynch and B.L. Iverson, *J. Org. Chem.* 2010, **75,** 7682–7690; c) J.J. Reczek, K.R. Villazor, V. Lynch, T.M. Swager and B.L. Iverson, *J. Am. Chem. Soc.* 2006, **128**, 7995-8002; d) T. He, M. Stolte, C. Burschka, N.H. Hansen, T. Musiol, D.l. Kalblein, J. Pflaum, X. Tao, J. Brill and F. Würthner, *Nature Comm.*, 2015*,* **6**, 5954; e) M. Diebold, E. Christ, L. Biniek, L. Karmazin, B. Heinrich, C. Contal, S. Ghosh, P. J. Mesini and M. Brinkmann, J. Mater. Chem. C, 2019, **7**, 13120-13129.

14 a) A. S. Raw, M. S. Furness, D. S. Gill, R. C. Adams, F. O. Holcombe and L. X. Yu, *Adv. Drug Delivery Rev*. 2004, **56**, 397-414; b) G. Goldbeck, E. Pidcock and C. Groom, *Solid Form Informatics for Pharmaceuticals and Agrochemicals: Knowledge-Based Substance Development and Risk Assessment*. CCDC, 2012 www.ccdc.cam.ac.uk/support-and-resources/ccdcresources/ Solid_Form_Informatics.pdf; c) J. Bernstein, *Polymorphism in Molecular Crystals*; Clarendon Press, Oxford, 2002.

15 O. D. Jurchescu, D. A. Mourey, S. Subramanian, S. R. Parkin, B. M. Vogel, J. E. Anthony, T. N. Jackson and D. J. Gundlach, *Phys. Rev.*, 2009, **80**, 0852012009.

16 a) R. Pfattner , M. Mas-Torrent, I. Bilotti, A. Brillante, S. Milita, F. Liscio, F. Biscarini, T. Marszalek, J. Ulanski, A. Nosal, M. Gazicki-Lipman, M. Leufgen , G. Schmidt, L. W. Molenkamp, V. Laukhin, J. Veciana and C. Rovira, *Adv. Mater.* 2010, **22**, 4198–4203; b) S. Galindo, A. Tamayo, F. Leonardi and M. Mas-Torrent, *Adv. Funct. Mater.* **2017**, *27*, 1700526-9; c) D. Gentili, M. Gazzano, M. Melucci, D. Jones and M. Cavallini, *Chem. Soc. Rev.*, 2019, **48**, 2502-2517.

17 Y. Matsunaga, K. Goto, K. Kubono, K. Sako, T. Shinmyozu, *Chem. Eur. J.* 2014, **20**, 7309-7316.

18 B. Schrode, S. Pachmajer, M. Dohr, V. Röthel, J. Domke, T. Fritz, R. Resel and O- Werzer, *J. Appl. Crystallogr*. 2019, **52** 683-689.

19 M. Cavallini, A. Calo, P. Stoliar, J.C. Kengne , S. Martins , F.C. Matacotta, F. Quist , G. Gbabode, N. Dumont , Y.H. Geerts and F. Biscarin, Adv. Mater. 2009, **21**, 4688-4691.

20 A. Calo, P. Stoliar, M. Cavallini, Y. H. Geerts and F. Biscarini, *Rev. Sci. Instrum.*, 2010, 81, #033907

21 P.M. Alvey, J.J. Reczek, V. Lynch and B. L. Iverson, *J. Org. Chem*. 2010, **75**, 7682–7690.

22 Y. Ofir, A. Zelichenok and S. Yitzchaik, *J. Mater. Chem*., 2016, **16**, 2142-2149.

23 O. Lukin, D. Schubert, C.M. Muller, W.B. Schweizer, V. Gramlich, J. Schneider, G. Dolgonos and A. Shivanyuk, *Proc. Nat. Acad. USA* 2009, **106**, 10922-10927.

24 A. Arduini, A. Credi, G. Faimani, C. Massera, A. Pochini, A. Secchi, M. Semeraro, S. Silvi, F. Ugozzoli, *Chem. Eur. J*. 2007, **14**, 98-106.

25 M.D. Curtis, J. Cao and J.W. Kampf. *J. Amer.Chem.Soc.,* 2004, **126**, 4318-4328.

26. A. M. Gueli, G. Bonfiglio, S. Pasquale and S. O. Troja, *Color Res. Appl.*, 2017, **42**, 236-243.

27 Y. Chino, K. Ohta, M. Kimura and M. Yasutake, *J. Porphyrins Phthalocyanines,* 2017, **21**, 159-178.

28 S. Himran, A. Suwono and G. Ali Mansoori, *Energy Sources J,* 1994, **16**, 117-128.

29 D.W.M. Hofmann, *Acta Cryst.* 2002, **B58**, 489-293.

30 K.J. Burch and E.G. Whitehead, Jr. *J. Chem. Eng. Data* 2004**, 49***,* 858-863.

31 D. Shukla, S.F. Nelson, D.C. Freeman, M. Rajeswaran, W.G. Ahearn, D.M. Meyer and J. T. Carey, *Chem. Mater.* 2008, **20**, 7486-7491.

32 E. Keller*, Chemie uns. Zeit* 1980, **14**, 56-60.

33 X.-Y. Wang and R. Salovey, *J. Appl. Polym. Sci.* 1987, **34**, 593-599.

34 D.W. Breiby, O. Bunk, J.W. Andreasen, H.T. Lemke and M.M. Nielsen, *J. Appl. Cryst.* 2008, **41**, 262-271.

35 J.A. Merlo, C.R. Newman, C.P. Gerlach, T.W. Kelley, D.V. Muyres, S.E. Fritz, M.F. Toney, C.D. Frisbie, *J. Am. Chem. Soc*. 2005, **127**, 3997-4009.

36 A.L. Spek, *Acta Cryst.* 2009, **D65**, 148-155.

37 A. Hammami and A.K. Mehrotra, *Fuel* 1995, **74**, 96-101.